Classification of Photospheric Emission in Short GRBs

Hüsne Dereli-Bégué[1,2] , Asaf Pe'er[2] , and Felix Ryde[3]

[1] Max Planck Institute for Extraterrestrial Physics, Giessenbachstrasse 1, D-85748 Garching, Germany; husnedereli@gmail.com
[2] Department of Physics, Bar-Ilan University, Ramat-Gan 52900, Israel
[3] Department of Physics, KTH Royal Institute of Technology, and The Oskar Klein Centre, SE-106 91 Stockholm, Sweden

Abstract

In order to better understand the physical origin of short-duration gamma-ray bursts (GRBs), we perform a time-resolved spectral analysis on a sample of 70 pulses in 68 short GRBs with burst durations $T_{90} \lesssim 2$ s detected by the Fermi/Gamma-ray Burst Monitor. We apply a Bayesian analysis to all spectra that have statistical significance $S \geqslant 15$ within each pulse and apply a cutoff power-law model. We then select in each pulse the time bin that has the maximum value of the low-energy spectral index for further analysis. Under the assumption that the main emission mechanism is the same throughout each pulse, this analysis is indicative of pulse emission. We find that about 1/3 of the short GRBs are consistent with a pure, nondissipative photospheric model, at least around the peak of the pulse. This fraction is larger than the corresponding fraction (1/4) obtained for long GRBs. For these bursts, we find (i) a bimodal distribution in the values of the Lorentz factors and the hardness ratios and (ii) an anticorrelation between T_{90} and the peak energy, $E_{\rm pk}$: $T_{90} \propto E_{\rm pk}^{-0.50 \pm 0.19}$. This correlation disappears when we consider the entire sample. Our results thus imply that the short GRB population may in fact be composed of two separate populations: one that is a continuation of the long GRB population to shorter durations, and another that is distinctly separate with different physical properties. Furthermore, thermal emission is initially ubiquitous, but is accompanied at longer times by additional radiation (likely synchrotron).

Unified Astronomy Thesaurus concepts: Gamma-ray bursts (629); Astronomy data analysis (1858); Gamma-ray astronomy (628)

1. Introduction

After more than four decades of extensive research, the physical origin of gamma-ray burst (GRB) prompt spectra remains unclear and highly debated. The classification of GRBs is a tool that might help understand the emission mechanisms at work. The main classification into short-hard and long-soft GRBs is based on their duration and spectral hardness. The duration of short GRBs is shorter than 2 s, and that of long GRBs is longer than 2 s (Kouveliotou et al. 1993). The spectral peak energy of short bursts is on average higher than that of long GRBs (e.g., Ghirlanda et al. 2011). However, the two classes share many spectral characteristics, for instance, their spectra peak in the MeV range, with power-law extensions below and above the peak. Both populations have a common inverse correlation between the intensity and the duration for individual pulses (Hakkila & Preece 2011; Norris et al. 2011), and they follow a similar relation between the peak energy, $E_{\rm pk}$, and the peak luminosity, $L_{\rm peak}$, as well as the isotropic equivalent energy, $E_{\rm iso}$, (Yonetoku et al. 2004; Amati 2006; Ghirlanda et al. 2009).

Despite these observed similarities, short and long bursts are thought to originate from different progenitors; the collapse of a very massive star for long GRBs (Woosley 1993) and a compact binary merger for short GRBs (Eichler et al. 1989). In fact, long GRBs are studied more than short GRBs. Indeed, they release more photons, which allows more detailed spectral studies. In addition, more redshifts are known for long than for short GRBs because the afterglow after a few thousand seconds is brighter for long bursts. This allows the study of intrinsic properties (e.g., Howell & Coward 2013). The recent increase of interest in the study of short GRBs is mostly due to the detection of the short GRB 170817B, which was made simultaneously with the detection of the first gravitational

wave from a merger of binary neutron stars (Abbott et al. 2017; Goldstein et al. 2017).

Observationally, many GRB prompt spectra have too narrow νF_ν peaks than expected from the synchrotron emission model (e.g., Ryde 2004; Axelsson & Borgonovo 2015; Yu et al. 2015). Yet, they are broader than a Planck spectrum (Goodman 1986; Paczynski 1986; Beloborodov 2011). Photospheric emission from highly relativistic outflows is often used to explain this observed spectral shape. The broadening of the spectrum by energy dissipation below the photosphere can be caused by shocks, dissipation of magnetic energy, or collisional processes (Giannios & Spruit 2005; Pe'er et al. 2006; Beloborodov 2010). Moreover, broadening in a passively cooled jet without any energy dissipation can be due to geometrical broadening that occurs during the coasting phase (Beloborodov 2011; Bégué et al. 2013; Lundman et al. 2013). In order for the emission to be detectable, the outflow has to become transparent below or close to the saturation radius, r_s, where the outflow saturates to its final outflow Lorentz factor (Mészáros 2006; Ryde et al. 2017).

The observed spectral shape of the prompt emission is commonly characterized by empirical models, such as the Band model (Band et al. 1993) or a cutoff power-law (CPL) model (see, e.g., Yu et al. 2016). However, in linking observation and theory, the parameters of the empirical models should not be used directly for the comparison with the prediction of physical emission models. Indeed, an attempt to make such a link leads to two main problems. The first problem is known as an energy-window bias effect. When the empirical model does not match the true spectral shape (its curvature, where a spectral peak lies inside the Gamma-ray Burst Monitor (GBM) energy window), then the physical interpretation of the model parameters will be wrong; e.g., there will be a positive

correlation between the parameters of the empirical model at low peak energies (e.g., Preece et al. 1998; Lloyd & Petrosian 2000; Burgess et al. 2015; Acuner et al. 2019; Ryde et al. 2019). The second problem is the limitation due to the bandwidth of the detector, which prevents the full spectrum from being detected (Burgess et al. 2015; Ryde et al. 2019).

There are two solutions to overcome these problems. The first solution is to use a physically motivated model and fit it directly to the data (e.g., Lloyd & Petrosian 2000; Ahlgren et al. 2015). In this way, there is no need for an empirical function. However, it is computationally expensive due to the need to make a forward-folding of the theoretically generated spectra through the detector's response matrix, and the need to subtract the background—both vary from burst to burst. Thus, the claimed model has to be fit individually to each burst. Furthermore, one has to assume knowledge of the physical model that should be used (e.g., Baring & Braby 2004; Burgess et al. 2016, 2019a; Oganesyan et al. 2019). Due to these limitations, this direct method was so far only applied to a limited number of bursts (e.g., Burgess et al. 2011; Vianello et al. 2018; Ahlgren et al. 2019).

The second solution is to use an assumed physical model to generate a large number of synthetic spectra that in turn are fit with empirical functions. This provides the distribution of the empirical model parameters that the given theoretical model corresponds to. The properties of the parameter distributions, for instance, their widths, depend on how well the empirical model matches the theoretical model. These distributions can then be compared to the full GRB catalog, in order to assess the ability of the theoretical model of explaining the data. This method was used by several authors (e.g., Burgess et al. 2015; Acuner et al. 2019) to make statistical claims about the ability of a theoretical model of fitting the data.

In an attempt to fit a nondissipative photospheric model (Beloborodov 2011; Lundman et al. 2013) to GRB spectra, Acuner et al. (2019) followed the second method and generated a series of synthetic spectra with a high signal-to-noise ratio (S/N) of 300 and peak energies at the range of 40–2000 keV. The simulated (synthetic) spectral data were fit with a CPL model. It was found that the distribution of the low-energy photon indexes ranges from -0.4 to 0.0 and peaks at around -0.1. This was then compared with the distribution of the maximum time-resolved value of the low-energy spectral index, $\alpha_{\max}$, in the samples of Yu et al. (2016, 2019). They found that $1/4$ of the long bursts have an $\alpha_{\max}$ that is consistent with a nondissipative outflow, releasing its thermal energy at the photosphere. However, Acuner et al. (2019) did not consider short bursts because the selection criteria of Yu et al. (2016, 2019) are mainly based on bright bursts with durations $T_{90} \gtrsim 2$ s.

While the spectral properties of short GRBs are much less studied than those of long GRBs, evidence is accumulating that photospheric (thermal) emission could play an important role in these bursts as well. The main motivation for our current study is the large number of short GRBs seen in cluster 5 in Acuner & Ryde (2018). This cluster was found to be consistent with a photospheric emission origin. Therefore, we here are also use the fitted synthetic spectra from Acuner et al. (2019) to find the fraction of short GRBs that is compatible with a nondissipative photosphere (NDP) model. As a first step, we apply a time-resolved analysis to the spectra of individual pulses obtained from 68 short GRBs and use a Bayesian analysis approach. As

a second step, we study in detail the time bins with the hardest low-energy spectral index ($\alpha_{\max}$) in each pulse.

This paper is organized as follows. In Section 2 we define the sample of short GRBs and present the analysis methods. In Section 3 we present the result of the spectral parameter relations, the observed α distributions, the Lorentz factor for the bursts consistent with thermal emission, and the hardness ratio (HR). In Section 4 we then discuss our choice of spectral fitting model, and the correlations between temporal and spectral structures. Finally, in Section 5 we list our summary and conclusions.

2. Data Collection and Analysis Method

2.1. Sample Selection

We select short GRBs, i.e., GRBs with a duration $T_{90} < 2$ s, detected by the GBM on board the Fermi Gamma-ray Space Telescope during the first 11 yr of its mission. We scan all the short bursts for which automatic spectral fits are performed on the time-resolved data around the peak flux within the time interval given in the GBM catalog (von Kienlin et al. 2014). We find a total of 147 short bursts for which spectral fits can be carried out and analyzed. All the data are taken from the Fermi/GBM burst catalog published at HEASARC.[4] We further set a limit for at least one time bin to have a statistical significance (see Section 2.2 for the definition) $S \geqslant 15$ in each pulse; we thus select 70 pulses from 68 short GRBs as a final sample. They are listed in Table 1.

2.2. Analysis Method

For the analysis, we follow the procedure of the Fermi/GBM GRB time-integrated (Goldstein et al. 2012; Gruber et al. 2014) and time-resolved catalogs (Yu et al. 2016, 2019). We select at most three sodium iodide (NaI) detectors and one bismuth germanium oxide (BGO) detector for the spectral analysis of each short GRB, see Table 1, Column 3. We use the response files RSP (except for two cases, GRB 090510 and GRB 170127, in which the RSP2 files are used) for each short GRB. We further use the standard Fermi/GBM energy ranges: 8–30 keV and 40 to $\sim$850 keV for the NaI detectors (avoiding the K edge at 33.17 keV),[5] and $\sim$250 keV to 40 MeV for the BGO detectors.

We select the source interval from the first few seconds of the burst light curve where the first pulse is most prominent; see Table 1, Column 4. Indeed, most of the bursts in the sample are single-pulsed bursts. We use the NaI detector in which the largest photon counts per second were recorded from the burst to define the background intervals before and after the pulse; see Table 1, Columns 3, 5, and 6, respectively. These intervals are then applied to all detectors. As a standard procedure in GRB background fitting of GBM data, we fit a polynomial with the order of between 0 and 4 to the total count rate of each energy channel (128 channels for time-tagged Events, TTE) of each detectors. From this fit, the optimal order of the polynomial is determined by a likelihood ratio test. Then, this order of polynomial is interpolated through the source time interval to estimate the background photon count flux and its corresponding errors in each energy channel during the time of source activity.

We then rebin the light curves by applying the Bayesian block method (Scargle et al. 2013) to the unbinned TTE data. This method identifies intervals that are consistent with a

---

Table 1
A Sample of 70 Pulses from 68 Short GRBs Used in This Study

bn	T_{90} (s)	Detectors	ΔT_{src} (s)	$\Delta T_{bkg,1}$ (s)	$\Delta T_{bkg,2}$ (s)	N	α_{max}	S	E_{pk} (keV)	Flux (erg cm^{-2} s^{-1})
081209981	0.19 ± 0.14	(n8)nbb1	-1.7 to 2.	$-20.$ to $-7.$	7. to 13.	5	$-0.42^{+0.09}_{-0.13}$	19	1080^{+190}_{-250}	$1.6^{+2.2}_{-0.9} \times 10^{-5}$
081216531	0.8 ± 0.4	n7(n8)nbb1	-1.7 to 2.	$-20.$ to $-7.$	15. to 35.	8	$-0.37^{+0.06}_{-0.07}$	30	1170^{+140}_{-110}	$1.6^{+1.1}_{-0.7} \times 10^{-5}$
081223419	0.58 ± 0.14	n6(n7)n9b1	$-2.$ to 2.	$-20.$ to $-7.$	15. t0 35.	4	$-0.42^{+0.13}_{-0.17}$	18	200^{+30}_{-50}	$2.0^{+3.4}_{-1.2} \times 10^{-6}$
090108020	0.71 ± 0.14	(n1)n2n5b0	$-2.$ to 2.	$-20.$ to $-7.$	15. to 35.	6	$-0.22^{+0.11}_{-0.15}$	25	140^{+10}_{-20}	$2.6^{+2.8}_{-1.3} \times 10^{-6}$
090227772	0.31 ± 0.02	n0(n1)n2b0	$-2.$ to 2.	$-20.$ to $-7.$	15. to 35.	9	$+0.07^{+0.07}_{-0.07}$	36	1720^{+110}_{-140}	$8.2^{+5.7}_{-3.4} \times 10^{-5}$
090228204	0.45 ± 0.14	(n0)n1n3b0	$-2.$ to 2.	$-20.$ to $-7.$	15. to 35.	11	$-0.01^{+0.06}_{-0.07}$	45	640^{+50}_{-50}	$13^{+10}_{-5.7} \times 10^{-5}$
090308734	1.67 ± 0.29	(n3)n6n7b0	$-2.$ to 2.5	$-20.$ to $-7.$	15. to 35.	6	$-0.42^{+0.09}_{-0.10}$	19	750^{+100}_{-160}	$3.0^{+3.6}_{-1.6} \times 10^{-6}$
090328713	0.2 ± 1.0	(n9)nanbb1	$-1.$ to 5.	$-20.$ to $-7.$	15. to 35.	3	$-0.87^{+0.06}_{-0.08}$	17	1700^{+310}_{-570}	$5.6^{+3.6}_{-2.4} \times 10^{-6}$
090510016	0.96 ± 0.14	(n6)n7n9b1	-1.7 to 2.	$-20.$ to $-7.$	15. to 35.	9	$-0.62^{+0.04}_{-0.05}$	32	2850^{+270}_{-340}	$2.1^{+1.0}_{-0.6} \times 10^{-5}$
090617208	0.19 ± 0.14	n0(n1)n3b0	$-1.$ to 2.5	$-20.$ to $-7.$	15. to 35.	4	$+0.05^{+0.18}_{-0.19}$	16	920^{+120}_{-310}	$1.1^{+3.7}_{-0.9} \times 10^{-5}$
090802235	0.04 ± 0.02	n2(n5)b0	$-3.$ to 8	$-20.$ to $-7.$	20. to 40.	4	$-0.48^{+0.14}_{-0.14}$	21	480^{+60}_{-100}	$1.4^{+2.7}_{-0.9} \times 10^{-5}$
090907808	0.8 ± 0.3	n6(n7)n9b1	$-2.$ to 2.	$-20.$ to $-7.$	15. to 35.	3	$-0.09^{+0.15}_{-0.16}$	17	450^{+60}_{-100}	$1.8^{+4.4}_{-1.2} \times 10^{-6}$
100223110	0.26 ± 0.09	n7(n8)b1	$-2.$ to 2.1	$-20.$ to $-7.$	15. to 35.	5	$-0.14^{+0.11}_{-0.12}$	20	1250^{+150}_{-260}	$0.9^{+1.4}_{-0.5} \times 10^{-5}$
100629801	0.8 ± 0.4	(na)nbb1	$-2.$ to 2.	$-20.$ to $-7.$	15. to 35.	5	$-0.76^{+0.15}_{-0.18}$	16	230^{+30}_{-80}	$2.8^{+5.6}_{-1.8} \times 10^{-6}$
100811108	0.39 ± 0.09	(n7)n9nbb1	$-2.$ to 2.	$-20.$ to $-7.$	15. to 35.	3	$-0.14^{+0.09}_{-0.11}$	19	1140^{+140}_{-220}	$6.9^{+8.2}_{-3.8} \times 10^{-6}$
100827455	0.6 ± 0.4	n6(n7)n8b1	$-2.$ to 2.	$-20.$ to $-7.$	15. to 35.	5	$-0.32^{+0.12}_{-0.11}$	16	780^{+110}_{-170}	$0.8^{+1.1}_{-0.5} \times 10^{-5}$
101216721	1.9 ± 0.6	n1n2(n5)b0	$-2.$ to 3.	$-20.$ to $-7.$	15. to 35.	8	$-0.54^{+0.08}_{-0.10}$	37	180^{+20}_{-20}	$3.2^{+2.5}_{-1.4} \times 10^{-6}$
110212550	0.07 ± 0.04	n6(n7)n8b1	-1.8 to 1.7	$-20.$ to $-7.$	15. to 35.	5	$-0.38^{+0.11}_{-0.14}$	18	620^{+90}_{-150}	$1.7^{+2.9}_{-1.0} \times 10^{-5}$
110526715	0.45 ± 0.05	(n3)n4b0	-1.7 to 2.	$-20.$ to $-7.$	15. to 35.	3	$-0.88^{+0.09}_{-0.10}$	17	670^{+110}_{-240}	$2.2^{+1.8}_{-1.0} \times 10^{-6}$
110529034	0.51 ± 0.09	n6n7(n9)b1	$-2.$ to 2.	$-20.$ to $-7.$	15. to 35.	10	$-0.52^{+0.15}_{-0.19}$	15	780^{+120}_{-350}	$1.0^{+2.4}_{-0.7} \times 10^{-5}$
110705151	0.19 ± 0.04	(n3)n4n5b0	-1.7 to 2.	$-20.$ to $-7.$	15. to 35.	8	$-0.09^{+0.11}_{-0.12}$	23	890^{+90}_{-180}	$1.6^{+2.2}_{-1.0} \times 10^{-5}$
111222619	0.29 ± 0.04	(n8)nbb1	$-2.$ to 2.	$-20.$ to $-7.$	15. to 35.	7	$-0.21^{+0.11}_{-0.12}$	27	700^{+70}_{-110}	$1.5^{+1.9}_{-0.8} \times 10^{-5}$
120222021	1.09 ± 0.14	n3n4(n5)b0	-1.7 to 2.	$-20.$ to $-7.$	15. to 35.	8	$-0.31^{+0.18}_{-0.26}$	34	120^{+20}_{-30}	$1.7^{+4.9}_{-1.2} \times 10^{-6}$
120323507	0.39 ± 0.04	n0(n3)b0	$-2.$ to 2.	$-20.$ to $-7.$	10. to 30.	16	$-0.73^{+0.15}_{-0.14}$	25	420^{+40}_{-160}	$3.1^{+5.6}_{-1.9} \times 10^{-5}$
120519721	1.1 ± 0.5	n7(n8)b1	-1.7 to 2.	$-20.$ to $-7.$	15. to 35.	6	$-0.45^{+0.09}_{-0.12}$	23	860^{+130}_{-190}	$3.9^{+5.5}_{-2.1} \times 10^{-6}$
120624309	0.64 ± 0.16	n1n2(na)b0	$-2.$ to 2.	$-20.$ to $-7.$	15. to 35.	11	$-0.68^{+0.05}_{-0.05}$	28	3590^{+370}_{-540}	$2.4^{+1.0}_{-0.7} \times 10^{-5}$
120811014	0.45 ± 0.09	n7(n8)b1	$-2.$ to 3.	$-20.$ to $-7.$	15. to 35.	5	$+0.01^{+0.12}_{-0.16}$	21	1170^{+180}_{-230}	$1.0^{+2.0}_{-0.6} \times 10^{-5}$
120817168	0.16 ± 0.11	n6(n7)n8b1	-1.5 to 1.7	$-20.$ to $-7.$	15. to 35.	6	$-0.50^{+0.06}_{-0.07}$	30	1530^{+190}_{-290}	$3.9^{+2.4}_{-1.5} \times 10^{-5}$
120830297	0.90 ± 0.23	(n0)n1n3b0	-1.7 to 2.	$-20.$ to $-7.$	15. to 35.	5	$-0.27^{+0.07}_{-0.10}$	24	1100^{+150}_{-180}	$3.6^{+3.2}_{-1.7} \times 10^{-6}$
121127914	0.6 ± 0.4	(n4)n8b1	$-2.$ to 2.	$-20.$ to $-7.$	15. to 35.	4	$-0.53^{+0.10}_{-0.11}$	19	1080^{+170}_{-270}	$6.6^{+8.8}_{-3.6} \times 10^{-6}$
130416770	0.2 ± 0.4	n3(n4)n5b0	-1.7 to 8.	$-20.$ to $-7.$	25. to 45.	3	$-0.52^{+0.08}_{-0.09}$	16	1100^{+170}_{-190}	$1.0^{+1.0}_{-0.7} \times 10^{-5}$
130504314	0.39 ± 0.18	(n3)n4b0	$-2.$ to 1.7	$-35.$ to $-7.$	15. to 30.	7	$-0.09^{+0.08}_{-0.11}$	21	1370^{+150}_{-190}	$1.4^{+1.7}_{-1.2} \times 10^{-5}$
130628860	0.51 ± 0.14	n7n9(nb)b1	$-2.$ to 2.1	$-20.$ to $-7.$	15. to 35.	7	$-0.18^{+0.14}_{-0.13}$	18	1120^{+150}_{-270}	$1.8^{+3.3}_{-1.1} \times 10^{-5}$
130701761	1.60 ± 0.14	(n9)nanbb1	$-2.$ to 3.	$-20.$ to $-7.$	15. to 35.	8	$-0.24^{+0.18}_{-0.05}$	18	1200^{+30}_{-330}	$4.4^{+8.6}_{-3.0} \times 10^{-6}$
130804023	0.96 ± 0.09	n6(n7)n9b1	$-2.$ to 2.	$-8.$ to $-5.$	12. to 29.	10	$-0.26^{+0.10}_{-0.10}$	20	850^{+109}_{-150}	$3.1^{+3.6}_{-1.7} \times 10^{-5}$
130912358	0.51 ± 0.14	n7(n8)nbb1	$-2.$ to 2.	$-20.$ to $-7.$	15. to 35.	8	$-1.02^{+0.08}_{-0.09}$	18	1700^{+230}_{-870}	$7.2^{+6.6}_{-3.4} \times 10^{-6}$
131126163	0.2 ± 0.4	n2(n5)b0	$-3.$ to 1.7	$-25.$ to $-10.$	15. to 35.	4	$-0.07^{+0.15}_{-0.16}$	19	750^{+100}_{-190}	$1.9^{+4.3}_{-1.3} \times 10^{-5}$
140209313	1.41 ± 0.27	n9(na)b1	0. to 4.	$-20.$ to $-7.$	20. to 40.	13	$-0.19^{+0.10}_{-0.10}$	44	220^{+20}_{-30}	$1.4^{+1.4}_{-0.7} \times 10^{-5}$
140807500	0.5 ± 0.2	n3(n4)n5b0	$-2.$ to 2.	$-20.$ to $-7.$	15. to 35.	4	$-0.75^{+0.07}_{-0.09}$	26	750^{+110}_{-190}	$5.2^{+4.0}_{-2.2} \times 10^{-6}$
140901821	0.18 ± 0.04	n9(na)nbb1	-1.5 to 2.	$-20.$ to $-7.$	15. to 35.	5	$-0.22^{+0.05}_{-0.06}$	36	1200^{+90}_{-100}	$2.5^{+1.3}_{-0.9} \times 10^{-5}$
141011282	0.08 ± 0.04	n0(n1)n9b0	-1.8 to 1.7	$-20.$ to $-7.$	15. to 35.	5	$-0.46^{+0.10}_{-0.11}$	20	790^{+100}_{-180}	$2.7^{+3.4}_{-1.4} \times 10^{-5}$
141105406	1.28 ± 1.03	n6n7(n9)b1	-1.7 to 2.	$-20.$ to $-7.$	15. to 35.	4	$-0.42^{+0.11}_{-0.13}$	18	500^{+70}_{-120}	$2.2^{+3.4}_{-1.4} \times 10^{-6}$
141202470	1.41 ± 0.27	(n7)n8nbb1	-1.7 to 3.	$-20.$ to $-7.$	15. to 35.	4	$-0.32^{+0.08}_{-0.10}$	20	840^{+110}_{-150}	$3.5^{+3.6}_{-1.7} \times 10^{-6}$
141213300	0.8 ± 0.5	n1(n2)n5b0	-1.7 to 2.	$-20.$ to $-7.$	15. to 35.	7	$-0.87^{+0.14}_{-0.16}$	15	210^{+30}_{-90}	$1.7^{+2.9}_{-1.0} \times 10^{-6}$
150118927	0.3 ± 0.1	n7n8(nb)b1	-1.7 to 1.7	$-20.$ to $-7.$	15. to 35.	6	$-0.65^{+0.08}_{-0.10}$	26	620^{+90}_{-160}	$1.4^{+1.4}_{-0.7} \times 10^{-5}$
150810485	1.3 ± 1.0	n6n7(nb)b1	-1.7 to 2.	$-20.$ to -7	15. to 35.	6	$-0.61^{+0.07}_{-0.08}$	15	1530^{+250}_{-360}	$5.4^{+4.4}_{-2.5} \times 10^{-6}$
150811849	0.64 ± 0.14	(n4)n5b0	$-2.$ to 2.	$-20.$ to $-7.$	15. to 35.	6	$-0.24^{+0.08}_{-0.11}$	18	1600^{+220}_{-270}	$8.3^{+9.3}_{-4.2} \times 10^{-6}$
150819440	0.96 ± 0.09	n2(na)b1	-0.2 to 0.3	$-20.$ to $-7.$	15. to 35.	9	$+0.25^{+0.14}_{-0.17}$	33	440^{+50}_{-70}	$6.2^{+12}_{-4.1} \times 10^{-5}$
150819440	0.96 ± 0.09	n2(na)b1	0.35 to 1.37	$-20.$ to $-7.$	15. to 35.	11	$-1.02^{+0.04}_{-0.05}$	71	330^{+30}_{-40}	$2.0^{+0.7}_{-0.5} \times 10^{-5}$
150922234	0.15 ± 0.04	n6(n9)nab1	-1.5 to 2.	$-20.$ to $-7.$	15. to 35.	7	$-0.24^{+0.16}_{-0.24}$	15	800^{+150}_{-270}	$1.1^{+4.3}_{-0.6} \times 10^{-5}$
150923864	1.79 ± 0.09	n6(n7)n9b1	$-2.$ to 3.	$-20.$ to $-7.$	15. to 35.	9	$+0.06^{+0.25}_{-0.21}$	15	140^{+20}_{-30}	$1.5^{+4.0}_{-1.1} \times 10^{-6}$
151222340	0.8 ± 0.4	(n4)b0	-1.7 to 2.	$-20.$ to $-7.$	15. to 35.	6	$-0.43^{+0.09}_{-0.12}$	16	1500^{+200}_{-320}	$4.6^{+6.6}_{-2.5} \times 10^{-6}$
151231568	0.8 ± 0.4	n6(n7)n8b1	-1.7 to 2.	$-20.$ to $-7.$	15. to 35.	6	$-0.58^{+0.10}_{-0.11}$	19	610^{+70}_{-180}	$4.1^{+4.7}_{-2.3} \times 10^{-6}$
160408268	1.1 ± 0.6	(n0)n1n3b0	-1.7 to 2.	$-20.$ to $-7.$	15. to 35.	3	$-0.77^{+0.08}_{-0.11}$	17	1070^{+180}_{-380}	$3.0^{+3.5}_{-1.5} \times 10^{-6}$
160612842	0.29 ± 0.23	n0(n1)b0	-1.7 to 1.7	$-20.$ to $-7.$	15. to 35.	4	$-0.78^{+0.08}_{-0.12}$	15	2150^{+510}_{-880}	$5.4^{+6.4}_{-2.6} \times 10^{-6}$
160726065	0.8 ± 0.4	n0(n1)n2b0	-1.7 to 2.	$-20.$ to $-7.$	15. to 35.	6	$-0.79^{+0.09}_{-0.13}$	21	460^{+70}_{-140}	$4.4^{+4.3}_{-2.0} \times 10^{-6}$
160806584	1.7 ± 0.5	(n8)nbb1	$-2.$ to 2.	$-20.$ to $-7.$	15. to 35.	6	$-0.41^{+0.14}_{-0.20}$	19	190^{+30}_{-50}	$2.1^{+4.8}_{-1.4} \times 10^{-6}$

Table 1
(Continued)

bn	T_{90} (s)	Detectors	ΔT_{src} (s)	$\Delta T_{bkg,1}$ (s)	$\Delta T_{bkg,2}$ (s)	N	α_{max}	S	E_{pk} (keV)	Flux (erg cm^{-2} s^{-1})
160822672	0.1 ± 0.4	n9(na)b1	$-2.$ to 1.7	$-20.$ to $-7.$	$15.$ to $35.$	5	$-1.26^{+0.03}_{-0.06}$	23	290^{+40}_{-50}	$12^{+4.5}_{-3.0} \times 10^{-5}$
170127067	0.13 ± 0.05	(n4)b0	$-2.$ to $2.$	$-35.$ to $-15.$	$35.$ to $55.$	5	$+0.43^{+0.16}_{-0.11}$	32	900^{+70}_{-90}	$5.1^{+12}_{-3.5} \times 10^{-5}$
170206453	1.17 ± 0.10	(n9)nanbb1	-1.7 to $3.$	$-20.$ to $-7.$	$15.$ to $35.$	9	$-0.13^{+0.07}_{-0.09}$	39	370^{+30}_{-40}	$1.5^{+1.2}_{-0.6} \times 10^{-5}$
170222209	1.67 ± 0.14	n2(n5)b0	-1.7 to $3.$	$-20.$ to $-7.$	$20.$ to $40.$	10	$-1.11^{+0.10}_{-0.13}$	15	1550^{+130}_{-1120}	$5.8^{+7.5}_{-3.3} \times 10^{-6}$
170305256	0.45 ± 0.07	n0(n1)n2b0	-1.7 to $2.$	$-20.$ to $-7.$	$15.$ to $35.$	6	$-0.23^{+0.11}_{-0.10}$	25	340^{+40}_{-50}	$7.9^{+8.0}_{-4.3} \times 10^{-6}$
170708046	0.15 ± 0.05	n7(n8)nbb1	-2 to 1.7	$-20.$ to $-7.$	$15.$ to $35.$	5	$-0.75^{+0.09}_{-0.10}$	23	310^{+40}_{-60}	$1.2^{+0.9}_{-0.6} \times 10^{-5}$
170816599	1.60 ± 0.14	n7(n8)nbb1	$-2.$ to $3.$	$-20.$ to $-7.$	$15.$ to $35.$	5	$-0.26^{+0.06}_{-0.07}$	26	1170^{+100}_{-120}	$1.1^{+0.6}_{-0.4} \times 10^{-5}$
171108656	0.03 ± 0.02	(na)nbb1	$-5.$ to 1.7	$-30.$ to $-10.$	$10.$ to $30.$	8	$-0.11^{+0.16}_{-0.18}$	25	120^{+10}_{-20}	$9.7^{+16}_{-6.3} \times 10^{-6}$
171126235	1.47 ± 0.14	n0(n1)n5b0	-1.7 to $3.$	$-20.$ to $-7.$	$15.$ to $35.$	9	$+0.09^{+0.14}_{-0.17}$	29	130^{+10}_{-20}	$4.4^{+6.2}_{-2.5} \times 10^{-6}$
180204109	1.15 ± 0.09	n3(n4)n5b0	$-2.$ to $2.$	$-20.$ to $-7.$	$15.$ to $35.$	12	$-0.75^{+0.12}_{-0.12}$	16	1300^{+180}_{-660}	$0.8^{+1.1}_{-0.4} \times 10^{-5}$
180703949	1.54 ± 0.09	n0n1(n3)b0	-0.30 to 0.68	$-20.$ to $-7.$	$20.$ to $40.$	8	$-0.35^{+0.10}_{-0.12}$	39	100^{+10}_{-10}	$4.7^{+3.6}_{-2.2} \times 10^{-6}$
180703949	1.54 ± 0.09	n0n1(n3)b0	0.7 to 2.5	$-20.$ to $-7.$	$20.$ to $40.$	12	$-0.24^{+0.06}_{-0.05}$	8	180^{+10}_{-10}	$1.5^{+0.6}_{-0.4} \times 10^{-5}$
180715741	1.7 ± 1.4	n3(n4)b0	$-2.$ to $3.$	$-30.$ to $-7.$	$20.$ to $45.$	5	$-0.31^{+0.16}_{-0.16}$	16	630^{+90}_{-220}	$1.8^{+4.0}_{-1.2} \times 10^{-6}$

Note. Column 1: GRB names (bn). Column 2: Burst duration. Column 3: Detectors; the brightest detector is in brackets and is used to determine background and Bayesian blocks. Column 4: Source interval. Columns 5 and 6: Background intervals. Column 7: Number of Bayesian blocks during the source interval. Column 8: Maximum low-energy spectral index. Column 9: Significance of the time bin with α_{max}. Column 10: Corresponding peak energy (E_{pk}). Column 11: Corresponding flux.

constant Poisson rate. The light curves are thus rebinned into intervals over which the intensity change is small. The method uses the probability of a false positive of an intensity change p_0, which we set to $p_0 = 0.01$.[6] This is the typical value employed for a GBM data analysis (e.g., Vianello et al. 2018; Burgess et al. 2019b; Yu et al. 2019). A consequence of the Bayesian block method is that the time bins will have variable widths and variable statistical significance. However, it ensures that the emission evolution is small within a time bin, which is essential in order to capture the instantaneous emission spectrum. We use the TTE data of the brightest NaI detector, and its binning is then transferred and applied to all other detectors. The total number of bins for each pulse is listed in Table 1, Column 7.

We further estimate the significance of the signal in each time bin. We employ the significance S given in Equation (15) in Vianello (2018), which is suitable for Poisson sources with Gaussian backgrounds. In particular, it is applicable for our analysis of GBM data because the background is not measured in an off-source interval, but is estimated through a polynomial fit, as described above. In this case, the typically employed S/N, given by $(n - b)/\sqrt{b}$, where n is the measurement and b is the background estimate, is not strictly valid and typically overestimates the significance measure (Vianello 2018). We find that the parameters from spectral modeling are typically well constrained when the statistical significance $S \geqslant 15$ (see the Appendix and Yu et al. 2019 for further details). Therefore, we limit our analysis to time bins with at least this level of significance.

For the spectral model, we use the CPL model, which is a power law with an exponential cutoff, which has been extensively used because it is the best model for most GRBs in the Fermi GBM catalogs (Goldstein et al. 2012; Gruber et al. 2014; Yu et al. 2016, 2019). The CPL fit parameters are the normalization K (ph s^{-1} cm^{-2} keV^{-1}), the low-energy

power-law index α, and the cutoff energy E_c (keV). We further derive the CPL peak energy E_{pk} (keV) and the CPL energy flux F (erg s^{-1} cm^{-2}).

To perform the time-resolved spectroscopy, we use the multi-mission maximum likelihood, 3ML, package (Vianello et al. 2015) and follow the method outlined in Yu et al. (2019). The spectral analysis is performed with a Bayesian approach. For the likelihood function we use a Poisson distribution for the source signal and a Gaussian distribution for the background signal. We employ prior distributions for the parameters that are based on the parameter ranges found in the GBM catalogs (e.g., Yu et al. 2016). While the normalization ($K \sim 10^{-11}$–10^3 ph s^{-1} cm^{-2} keV^{-1}) is assumed to have a log uniform prior, the low-energy index ($\alpha \sim -3$ to 2) and the cutoff energy ($E_c \sim 10$–10,000 keV) are assumed to have uniform priors. We also investigate the sensitivity to the prior choices by trying different distributions of the priors. We find that the fit results are insensitive to the choice of prior distributions, mainly due to the high-significance level of the data that we are analyzing. A similar conclusion was drawn by Acuner et al. (2020).

The spectral analysis yields posterior probability distributions of the parameters by using their prior probability distributions and the likelihood function obtained from the data. For this, we used the Markov chain Monte Carlo (MCMC) technique. All parameter uncertainties quoted in this paper are characterized by the highest posterior density credible intervals.

3. Spectral Analysis Results

3.1. Parameter Relations: The Entire Sample

In the 68 short GRBs listed in Table 1, we identified 70 distinct pulses. When divided into separate time bins, a total of 475 spectra within the GBM energy range (8 keV–40 MeV) can be analyzed. Out of these, 153 spectra have a statistical significance $S \geqslant 15$. The results of the CPL model fits to these 153 spectra are presented in Figure 1. We show several of the relations: $\alpha - E_c$ (upper left panel), $\alpha - E_{pk}$ (upper right panel), $F - E_{pk}$ (bottom left panel), and $F - \alpha$ (bottom right

---

[6] The exact value of p_0 is determined through a tradeoff between the risk of identifying noise fluctuations versus missing real intensity changes. It needs to be found through an iterative method, but is not very sensitive for data with even moderate significance (Scargle et al. 2013).
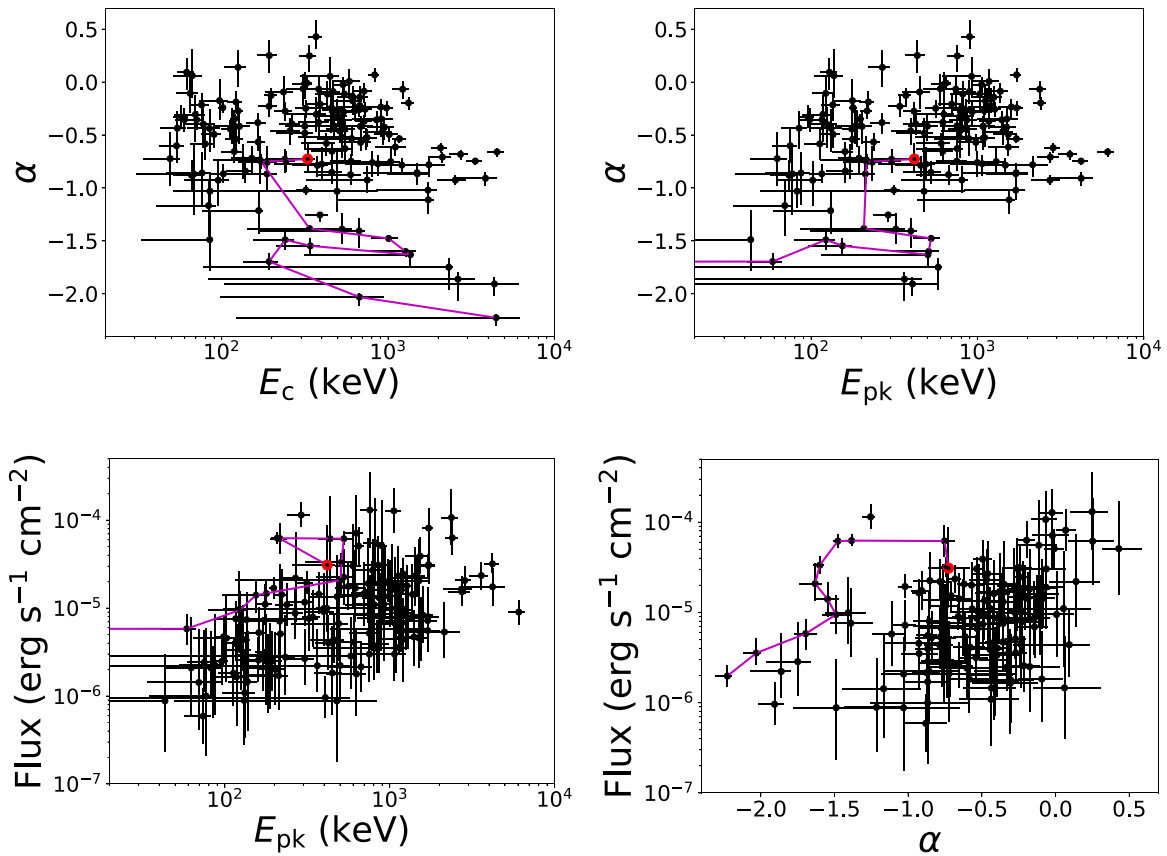
Figure 1. Global relations of the fitted parameters within the GBM energy range (8 keV–40 MeV) for time bins with a statistical significance $S \geqslant 15$. For the definition of parameters, see Section 2.2. We only see a trend of a positive correlation between F–E_{pk}. The purple lines follow the time evolution of the brightest short GRB 120323, starting with the first time bin in red.

panel). We only observe a trend of a positive correlation between $F - E_{pk}$ (Figure 1, bottom left panel).[7]

We point out that most of the data with a very low spectral index $-2.1 < \alpha < -1.1$ belong to a single burst, the brightest short GRB 120323 (see Figure 1). As a result, the values of α for the vast majority of bursts in our sample lie between -1.6 and $+0.6$ within 1σ uncertainty. This range is narrower than that observed in long GRBs, $-2 < \alpha < 1$ (Yu et al. 2019). However, the range of E_{pk} (40 keV $< E_{pk} < 6$ MeV) and flux (8×10^{-6} erg s^{-1} cm^{-2} $< F < 9 \times 10^{-3}$ erg s^{-1} cm^{-2}) obtained from short GRBs is similar to the range obtained in long GRBs, 10 keV $< E_{pk} < 7 \times 10^3$ keV and 10^{-7} erg s^{-1} cm^{-2} $< F < 5 \times 10^{-5}$ erg s^{-1} cm^{-2} (Yu et al. 2019).

When the results presented in Figure 1 are compared to the results obtained by Yu et al. (2019), we conclude that most of the bins obtained from short GRBs generally have harder values of the spectral index α, higher energies, and higher fluxes than those in long GRBs.

3.2. Distribution of Low-energy Spectral Indexes

We show the distribution of the low-energy spectral indexes, α, in the left panel of Figure 2. The histogram contains 153 spectra. The green curve is a smoothed version of the distribution, using the kernel density estimation (KDE), for which the errors are taken into account (see Silverman 1986 for

the KDE definition). We use the average of the asymmetric errors as the standard deviation of the Gaussian kernels in the KDE. This is a reasonable choice because the highest posterior density credible intervals of the α parameter are roughly symmetric around its mean values. We compare the values of the low-energy spectral index α (considering 1σ lower limit) with the synchrotron line-of-death value (Preece et al. 1998; Kaneko et al. 2006) $\alpha = -2/3$, which is shown by the red dashed line in Figure 2. We find that 56% of the analyzed spectra (within a 1σ error) violate the criteria set by the synchrotron line-of-death.

Global parameter distributions, such as this α-distribution, contain a varying number of spectra from each individual burst, and the spectral index typically varies between time bins of the same burst. Therefore it is difficult to draw firm conclusions on the emission mechanism based on the entire sample because there is a bias toward strong bursts with many time bins (e.g., GRB 120323; see the purple line in Figure 1).

The best way to constrain the emission mechanism during a pulse/burst therefore is to select the time bin that contains the highest value of the spectral index α in each pulse/burst. The reason for this is that physical models typically have an upper limit on how hard the spectra can become. Therefore it is enough that one single bin violates such a limit for the corresponding emission model to be rejected by the data, under the assumption that a single emission mechanism is the source of the observed signal in the entire duration of the burst (e.g., Acuner et al. 2019; Ryde et al. 2019; Yu et al. 2019). Some time-resolved spectral catalogs present the evolution of the

---

[7] When we remove the brightest short GRB 120323, we see a weak correlation between F and α, with α the Spearman rank correlation coefficient $r = 0.4$. This means that the chance probability is $p = 8.4 \times 10^{-7}$.
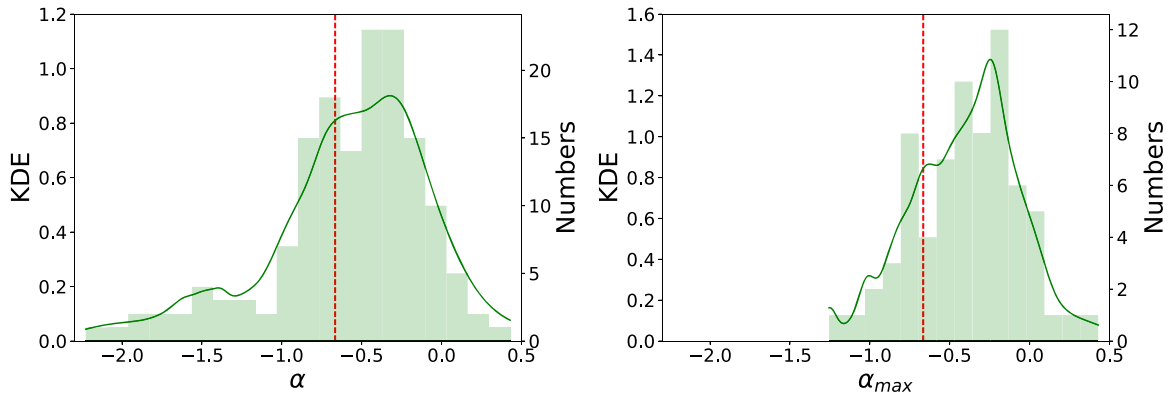
Figure 2. Distribution of the spectral index α of two different samples. Left panel: The α-distribution from 153 spectra obtained from the 70 pulses in 68 short GRBs. Right panel: Distribution of the the maximum (hardest) value of α, denoted α_{max}, in each of the 70 pulses. The red dashed lines indicate the line-of-death, $\alpha = -2/3$, for synchrotron emission. In both panels the right-hand ordinate is the number of spectra in each histogram bin and the left-hand ordinate is the value of the KDE, which is shown by the green curves. The KDE uses Gaussian kernels in which the standard deviation is set to the average of the asymmetric errors (see Silverman 1986 for the KDE definition).
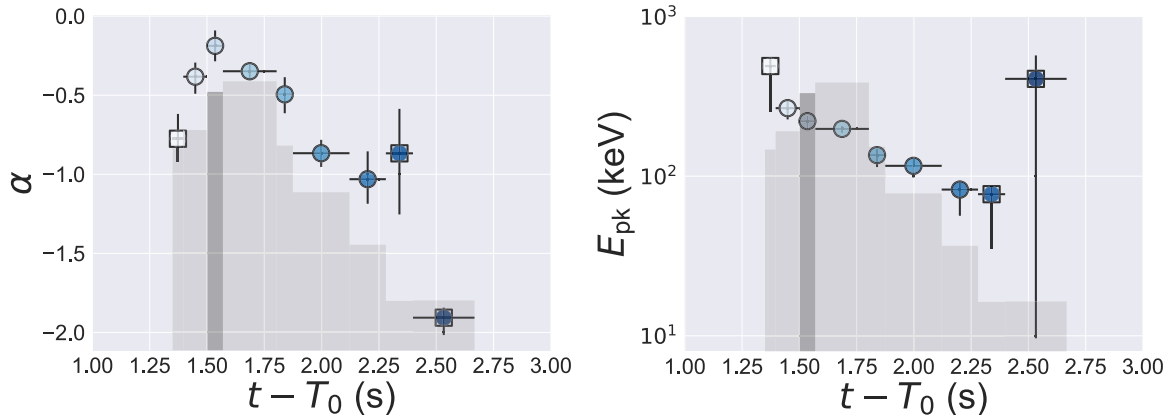
Figure 3. Spectral evolution of GRB 140209 shown as an example. The spectral index α (left panel) and the peak energy E_{pk} (right panel) are shown together with the energy flux light curve (in arbitrary logarithmic units) overlaid in gray. Only the time bins (from light to dark blue) with a statistical significance $S \geqslant 15$ are shown. Data points with circles indicate a statistical significance $S \geqslant 20$. In left panel, the spectral index α peaks close to the peak of the light curve. This is the typical behavior of most pulses (Ryde et al. 2019; Yu et al. 2019). The α_{max} time bin is marked in dark gray.

parameters over all time bins (e.g., Kaneko et al. 2006; Yu et al. 2016, 2019). Their parameter relations for individual GRBs are then interpreted by physical models (e.g., a qualitative photospheric emission scenario, Ryde et al. 2019).

For each of the 70 pulses in the 68 short bursts in our sample we therefore select the time bin that contains the maximum (hardest) value of the low-energy spectral index, which is denoted by α_{max}. The spectral index α_{max} and its corresponding peak energy (E_{pk}), flux, and statistical significance (S) are listed in the last four columns of Table 1. We find that for most pulses, α_{max} occurs close to or at the peak of the light curve. As such, it contains the most valuable information of the spectra. This is demonstrated in GRB 140209 shown in Figure 3: the temporal evolution of α and of the peak energy E_{pk} are shown, overlaid on the energy flux light curve in gray.

We now show in Figure 2 (right panel) the distribution of α_{max} in each of the 70 pulses from 68 short GRBs in the sample together with the KDE of the distribution. The red dashed line again shows the synchrotron line-of-death, $\alpha = -2/3$. We find that 70% (within a 1σ error) of the pulses violate the line-of-death criterion, and are therefore better interpreted with a model that is not synchrotron, such as the photospheric model. This fraction is larger than the fraction obtained in the case of

long GRBs, 60% within a 1σ error (Yu et al. 2019). We also note that the softest value is $\alpha_{\mathrm{max}} = -1.26$ for GRB 160822.

3.3. On the Consistency with the Nondissipative Photospheric Model

We show in Figure 4 the relation of α_{max} and E_{pk} in all 70 pulses from 68 short GRBs in the sample. The light blue line corresponds to the values of α that are found when a CPL function is fit to synthetic data, generated by an NDP spectrum peaking at different energies, E_{pk}, as described in Acuner et al. (2019) and shown in their Figure 3. These α-values (light blue line) are significantly lower than the asymptotic slope of the theoretical NDP spectrum ($\alpha \sim 0.4$, Beloborodov 2010; Bégué et al. 2013; Ito et al. 2013; Lundman et al. 2013) due to (i) the limited energy band of the detector and (ii) the limitation of the CPL function to correctly model the shape of the true spectrum. The shape of the NDP is shown in Figure 1 in Ryde et al. (2017), and an analytical approximation is given in Equation (1) in Acuner et al. (2019).

From Figure 4, we find that 36% of the observed points (25/70) are consistent with being above the NDP line within 1σ error, and are therefore consistent with having a dominant quasi-blackbody component. This fraction is significantly larger than
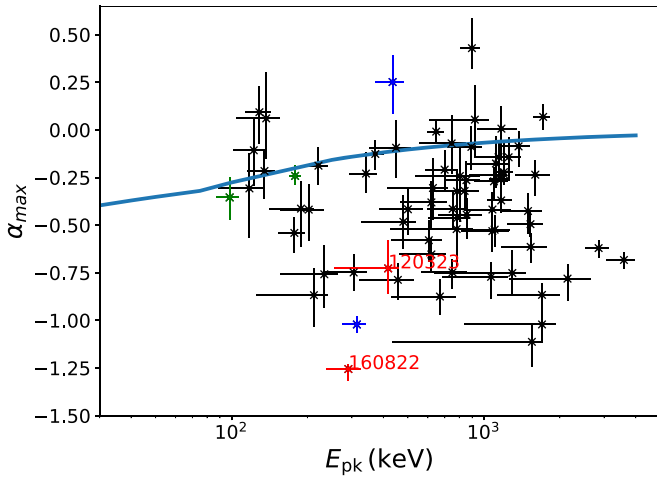
Figure 4. Relation of α_{max} and E_{pk} for 70 pulses from 68 short GRBs. The light blue line is the expectation from an NDP spectrum (see Section 3.3 for the definition). The fraction of pulses with α_{max} larger than the NDP model prediction is 36% (25 out of 70 pulses) within 1σ error. The blue and green points are for GRB 150819 and GRB 180703, which both have two pulses. GRB 120323 (which is the brightest short GRB) and GRB 160822 (which has the softest value of α_{max}) are shown in red.

the fraction found in the study of pulses from long GRBs, 26% (for single or multiple pulses bursts) and 28% (for only single-pulsed bursts) from the two catalogs of Yu et al. (2016, 2019), respectively; see Acuner et al. (2019) for further details.

Even though most of the short GRBs in the sample are single-pulse bursts, two bursts in our sample (GRB 150819 and GRB 180703) are found to have two separate pulses (these are marked by blue and green points, respectively, in Figure 4). While the first pulse of GRB 150819 (blue in Figure 4) shows a hard spectral index, $\alpha_{\mathrm{max}} = 0.25^{+0.14}_{-0.17}$, the spectral slope of the second pulse is much softer, $\alpha_{\mathrm{max}} = -1.02^{+0.04}_{-0.05}$. This might be an indication for a change in leading emission mechanism, e.g., from photospheric emission to synchrotron (Zhang et al. 2018). On the other hand, both pulses of GRB 180703 (green in Figure 4) are very hard, and they are both compatible with the NDP line. This might be an example of a burst in which a single emission mechanism is responsible for the full duration of a burst. In this case, the dominant emission mechanism throughout the full duration of the burst is likely photospheric emission (Acuner & Ryde 2018).

3.4. Lorentz Factor

If indeed the observed spectra above the NDP line have a photospheric origin, then one can use the data to calculate the coasting Lorentz factor, η. Here we estimate the Lorentz factor, η, for 25 pulses from 24 short GRBs above the NDP line by using Equations (1) and (4) in Pe'er et al. (2007). As the redshifts of most bursts in our sample are unknown, we have assumed redshift $z = 1$. We further assume that the flux, F, in the analyzed time bin is equal to the blackbody flux, $\sim F_{\mathrm{BB}}$, and that the observed temperature is related to the peak energy via $E_{\mathrm{pk}} \sim 1.48 T^{\mathrm{obs}}$. The flux and peak energy (E_{pk}) for each short GRB obtained in our analysis for the corresponding α_{max} time bin are presented in Table 1. For comparison, we also compute η for all 12 long GRBs found above the NDP line in the samples of Yu et al. (2019) and Acuner et al. (2019).

The distributions of the Lorentz factor η for 25 pulses from 24 short GRBs and 12 long GRBs above the NDP line are presented

in Figure 5. We find that the mean Lorentz factor ($\eta_{\mathrm{mean}} = 775$) of the short GRBs is similar, although somewhat higher, than that of the long GRBs ($\eta_{\mathrm{mean}} = 416$) (Pe'er et al. 2007; Racusin et al. 2011; Chen et al. 2018; Ghirlanda et al. 2018).

Surprisingly, we find a bimodal distribution in the values of η for short GRBs (Figure 5, left panel). There are 11 objects in peak 1 and 14 objects in peak 2. However, no such bimodal distribution is found in the analysis of long GRBs. The low peak coincides with the values obtained for long GRBs, while the high peak is a factor of ~ 3 higher. When we cut the sample at $\eta_c = 700$, we find that the pulses with high Lorentz factors, defined as peak 2, have a correspondingly higher E_{pk} (Figure 5, right panel). While this by itself may not be surprising, we point out that no such clear correlation is observed when the entire population of 70 pulses is analyzed (see Figure 4).

To validate the existence of this bimodality, we applied the dip test (Hartigan & Hartigan 1985) in the R package[8] to the sample of 25 pulses. The dip test results in 0.092, implying that the Lorentz factor distribution is bimodal at a confidence level of 95%.

3.5. Correlations in Bursts above the NDP Line

For the two groups from the bimodal η distribution (Figure 5), a strong positive correlation between η and E_{pk} is found (Figure 6, top left panel). This can be explained as due to the computational dependence, as $\eta \sim E_{\mathrm{pk}}^{1/2} F^{1/8}$, where F is the flux in each of the analyzed time bins. The formula is adopted from Pe'er et al. (2007) by identifying the peak energy with the blackbody temperature. The full dependence is $\eta \sim E_{\mathrm{pk}}^{1/2} F^{1/8} (1 + z)^{1/2} d_L^{1/4}$. Therefore, it is important to note that the computation is not very sensitive to the uncertainty on the distance.

However, unexpectedly, we also find anticorrelations between η and T_{90} and between T_{90} and E_{pk} (Figure 6). The latter correlation is between observed quantities and thereby independent of any model for deriving their values, unlike η. We therefore fit this correlation with a power-law function $T_{90} \propto E_{\mathrm{pk}}^{-s}$ using Bayesian inference and account for the measurement errors in both parameters. We make use of MCMC algorithms to explore the posterior distribution of the fit (see, e.g., Kelly 2007). This is shown by the gray lines (Figure 6, bottom left panel) which are 1000 randomly selected samples from the MCMC sampling and shows the degree of spread in the posterior distribution of the slope. The blue line shows the mean of the posterior distribution and has a slope of $s = 0.50$. The corresponding standard deviation 0.19.

We do not observe any correlation between T_{90} and the spectral slope α_{max} for bursts above the NDP line (Figure 6, bottom right panel). Similarly, no such correlation is found when the entire sample of 70 pulses is considered. However, when we consider all the sources having $E_{\mathrm{pk}} > 800\,\mathrm{keV}$ (presented in Figure 4), we do observe an anticorrelation between T_{90} and α_{max}, which is presented in Figure 7. This anticorrelation implies that sources with harder spectra have shorter T_{90}. This suggests that there might always exist a thermal emission at short times that is accompanied by other emission processes such as synchrotron at later times. If this interpretation is correct, the lack of thermal emission in a given GRB might be explained by the lack of observed or studied spectra at sufficiently short time.
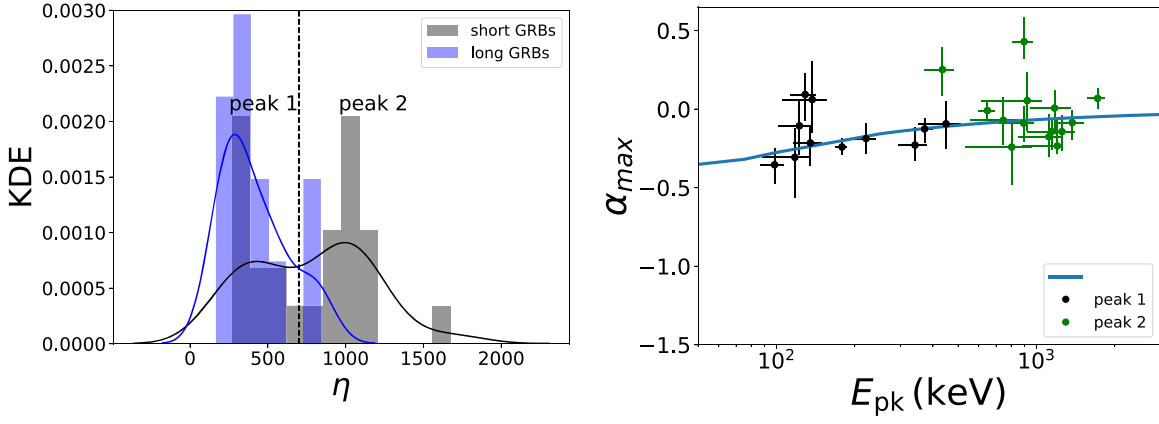
---

[8]　https://github.com/alimuldal/diptest

Figure 5. Left: Distributions of the Lorentz factor, η, for 25 pulses from 24 short GRBs (black histogram) and 12 long GRBs (blue histogram) above the NDP line. The curves represent the KDE of the distributions. The black dashed line indicates a cut at $\eta_c = 700$ to show the transition between peak 1 and peak 2 in the bimodal distribution of short GRBs. Right: α_{max} and E_{pk} relation (the Spearman rank correlation coefficient is $r = 0.29$, the chance probability is $p = 0.16$). Data points are the short GRBs from the bimodal η distribution (peak 1: black, and peak 2: green). The light blue line (NDP line) is the same as in Figure 4.
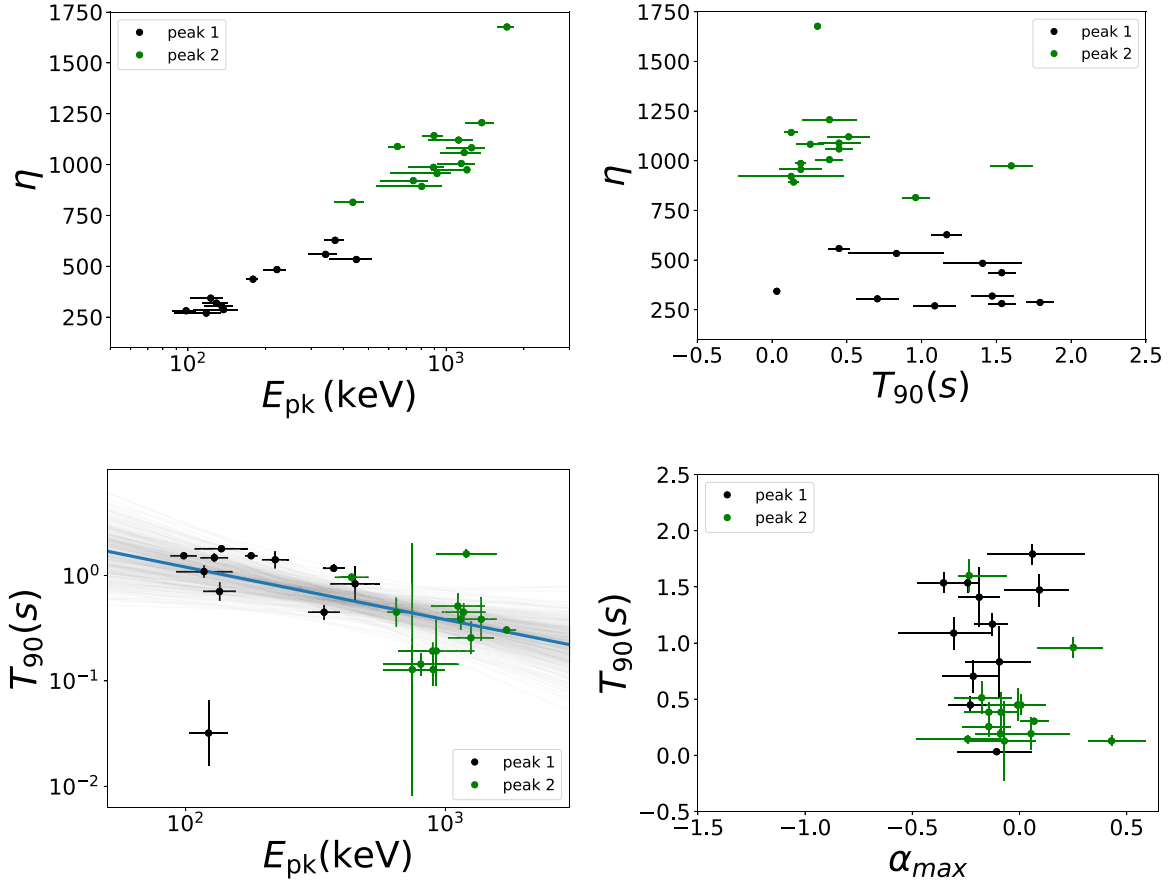
Figure 6. Parameter relations for the 25 pulses in our sample that lie above the NDP line. The black and green data points correspond to the two peaks in the η distribution defined in Figure 5. Upper left panel: relation of η vs. E_{pk}, which has a Spearman rank correlation coefficient $r = 0.92$, corresponding to a chance probability of $p \ll 0.00001$. Upper right panel: relation of η vs. T_{90} ($r = -0.53$, $p = 0.01$). Bottom left panel: relation T_{90} vs. E_{pk} ($r = -0.43$, $p = 0.03$). In this case, we fit for the correlation with a power-law function $T_{90} \propto E_{pk}^{-s}$ using Bayesian inference. The light blue line shows the mean of the posterior distribution (with a slope of $s = 0.50$ and a corresponding standard deviation of 0.19), and the gray lines are 1000 randomly selected samples from the MCMC sampling, which shows the degree of spread in the posterior distribution of the slope. Bottom right panel: relation T_{90} vs. α_{max} ($r = -0.28$, $p = 0.18$).

3.6. Hardness Ratio

The anticorrelation we found between E_{pk} and T_{90} of short GRBs with high E_{pk} motivated us to study a possible correlation between the HR and T_{90}. Following Kouveliotou

et al. (1993), we calculate the HR using the two typical energy bands, 100–300 and 50–100 keV. To integrate the spectra, we use the CPL fit parameters, α_{max} and E_c, for the 70 spectra in our sample. For comparison, we also calculated the HR for the
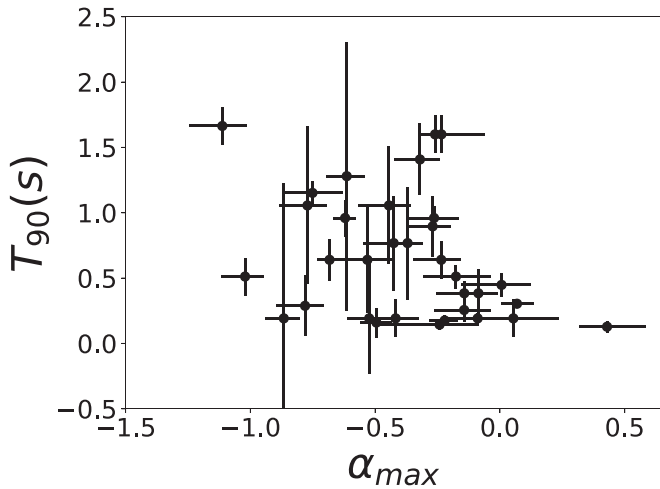
Figure 7. T_{90} and α_{max} relation for spectra with $E_{pk} > 800$ keV in Figure 4. The Spearman rank correlation coefficient is $r = -0.37$, and the chance probability is $p = 0.03$.

spectra with the maximum value of α in each of the 38 pulses from 37 long GRBs in the catalog by Yu et al. (2019). These pulses were selected from single-pulsed long bursts that have at least five time bins in which the statistical significance is $S \geqslant 20$.

The HR–T_{90} relation is shown in Figure 8 (left panel) for both short and long GRBs. Short bursts with α_{max} above the NDP model prediction are displayed in black while those below the prediction are plotted in red. For the long bursts, the colors are blue and purple, respectively. While the T_{90} selection criteria enable us to clearly discriminate the long and short GRB population, we do not observe any additional correlation in this plot.

The HR–T_{90} relation for the 25 pulses from 24 short GRBs above the NDP line is shown in the right panel in Figure 8. The color-coding (peak 1: black, and peak 2: green) is the same as that used for the bimodal η distribution in Figure 5. Now, a clear separation is observed: GRBs with lower peak energy have a low Lorentz factor, lower HR, and longer T_{90}.

Indeed, all the parameters of these GRBs in the first peak of the bimodal η distribution (in Figure 5, black) seem to form a continuous distribution of the parameters of the population of long GRBs. This is in contrast to GRBs in the second peak of the bimodal η distribution (in Figure 5, green), which have a higher HR than the GRBs below the NDP line (45 pulses) and long GRBs (38 pulses). This result implies that the duration T_{90} as a single criterion does not make a good separation between the two populations; as we show, the short GRBs may instead be composed of two separate populations, one that forms a continuation of the long GRB population, and another, separate population.

3.7. Spectral Parameter Correlations for the Two Groups

We find a weak positive correlations between F and E_{pk} (in Figure 9, left panel) and between F and α_{max} (in Figure 9, right panel) for bursts above the NDP line (in the two groups seen in the bimodal η distribution). However, no clear correlation is seen between these parameters for the bursts below the NDP line. This by itself is an interesting result. In the literature, several publications claim that there is a strong correlation between the luminosity, L_{peak}, or the isotropic energy, E_{iso}, and peak energy,

E_{pk} (e.g., Yonetoku et al. 2004; Amati 2006; Ghirlanda et al. 2009). These claims are based on a large sample of long GRBs. In contrast, here we do not find any such correlation when the entire sample of short GRB pulses is considered, but we do find a correlation when we consider only those short GRBs whose spectral slope are above the NDP line.

4. Discussion

4.1. On the Choice of the Fitted Model

In this work, we fit the Fermi/GBM data using the phenomenological CPL model (this is also known as the Comptonized model). Several empirical models are commonly used in the literature for the spectral analysis of GRBs. In addition to the CPL model (Kaneko et al. 2006), these include the Band model (Band et al. 1993) as well as the smoothly broken power-law model (Ryde 1999). Yu et al. (2016) showed that the CPL is the preferred model for the majority (70%) of bursts, according to the Castor C-Statistic (CSTAT).[9] In addition, a consistent result was found by Yu et al. (2019) based on the deviance information criterion (DIC) in Bayesian statistics (Spiegelhalter et al. 2002). This means that the results of the CPL model for these bursts have lower DIC and higher effective number of parameters, $p_{DIC} > 0$ (Gelman et al. 2014), than those of the Band model. Additionally, the resulting parameters for the CPL fits are constrained within the prior ranges more often than those obtained from the BAND function fits; see also Burgess et al. (2019a, 2019b).

It was recently argued by Burgess et al. (2019a) that a direct fit of the data to a synchrotron model enables overcoming the line-of-death criteria in many GRBs. However, this idea suffers several severe drawbacks. First, the bursts selected in that work are limited to bursts in the Yu et al. (2016) catalog, with the additional constraints of being single-pulse GRBs and having known redshifts. This selection is different from the short pulses considered here. Second, the values of the parameters found in their fits require an unacceptably high ratio of explosion energy to ambient mass density, of more than 7 orders of magnitude higher $(E/10^{53}$ erg$)/(n_{ism}/1$ cm$^{-3}) \gtrsim 4 \times 10^7$ than the highest observed so far. In order to overcome this problem, Burgess et al. (2019a) suggested an additional acceleration of particles within the relativistically expanding jet ("jet within a jet"); however, no such mechanism that can lead to relativistic expansion within an already relativistically expanding jet is known. We thus find that this model is still incomplete, and an interpretation of an empirical fit still provides better insight. Another suggestion was given by Ghisellini et al. (2020) based on the low-energy break in the prompt spectrum of GRBs. They argued that the emission process is still synchrotron radiation, but produced by protons, and that it cannot be completely cool.

4.2. Correlation between Temporal and Spectral Structures

When we consider the entire sample of 70 pulses analyzed in the short GRB population, we do not observe a correlation between the burst duration T_{90} and the peak energy E_{pk}. Similarly, for the long GRBs that we considered (both below and above the NDP line), no clear $T_{90} - E_{pk}$ correlation was detected. However, when we consider only those short bursts

---

[9] CSTAT is a modified version of the original Cash statistic (Cash 1979) in the case of Poisson data with Poisson background. Unlike the Cash statistic, it is used to determine an approximate goodness-of-fit measure to a given value of the CSTAT statistic.
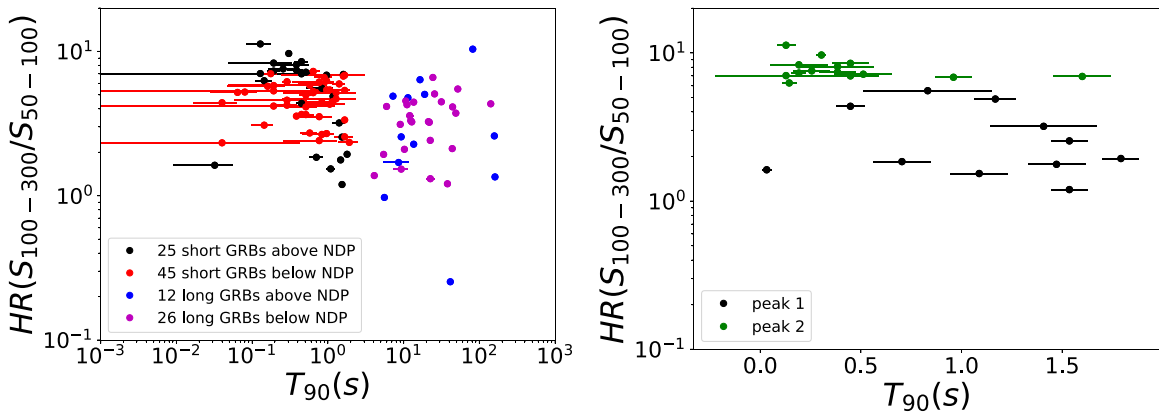
Figure 8. HR vs. pulse (burst) duration (T_{90}). Left panel: 70 pulses from 68 short GRBs (red and black) and 38 pulses from 37 long GRBs (blue and purple). Right panel: 25 pulses from 24 short GRBs, all lying above the NDP line (the black and green data points correspond to the two peaks in the η distribution defined in Figure 5). The Spearman rank correlation coefficient is $r = -0.56$, and the chance probability is $p = 0.01$.
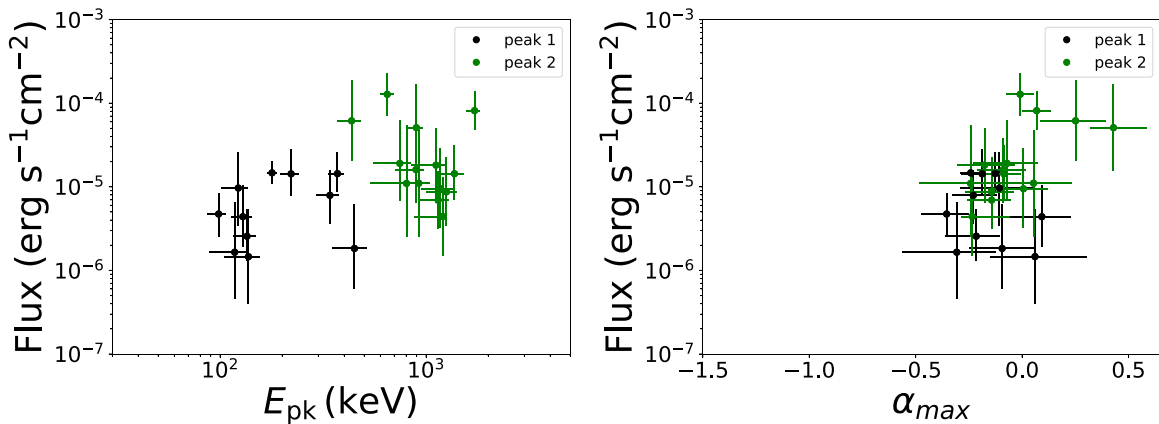

Figure 9. Flux dependencies for spectra above the NDP line (the black and green data points correspond to the two peaks in the η distribution defined in Figure 5). Left panel: Flux vs. E_{pk} ($r = 0.40$ and $p = 0.05$). Right panel: Flux vs. α_{max} ($r = 0.39$ and $p = 0.06$).

that have a hard value of the spectral index, α, such that they are above the NDP line (Figures 4, 5), we do find an inverse correlation between T_{90} and peak energy, $T_{90} \propto E_{pk}^{-s}$, where the slope of the power-law function is $s = 0.50$ and the corresponding standard deviation is 0.19.

A quantitative relationship between the temporal and spectral structure in GRBs has been considered by several authors in the past. However, these works treated only the long GRBs. Richardson et al. (1996) and Bissaldi et al. (2011) found a negative correlation between T_{90} and peak energy, $T_{90} \propto E_{pk}^{-s}$ where $s \simeq 0.4$. Their samples contained only the bright, long GRB population. When considering the entire set of the long GRB population, Qin et al. (2013) report a similar correlation, but with weaker dependence, $s = 0.2$.

Here we report for the first time such a correlation in the sample of short GRBs. This could not have been done in the past because the sample was small, and because a suitable method for studying the spectra was lacking. The similarity between the correlation found here for short GRBs above the NDP line and for the bright long GRBs (which tend to have a harder spectral index, α; see Bissaldi et al. 2011), as well as the fact that we do not detect any correlation for bursts below the NDP line, suggests a possible correlation between the emission mechanism and the burst duration. Bursts above the NDP line are consistent with originating from the photosphere, hence the

photons directly probe the inner engine. In contrast, bursts whose spectra are below the NDP line may have additional radiative mechanisms, such as synchrotron emission, which originate from the outer regions of the outflow (outside the photosphere) and as such do not necessarily directly follow the duration of the inner engine. If this interpretation is correct, it points to a possible correlation between the duration of the inner engine and the temperature, or total energy, of the released photons. This further points to the importance of a spectral analysis in analyzing possible correlations in the GRB population.

A second correlation we find is between T_{90} and α_{max} when we consider a cut at higher peak energy ($E_{pk} > 800$ keV) (see Figure 7). This (anti-) correlation further suggests a dual emission mechanism: short-duration GRBs might be dominated by a thermal component, while an additional emission process may lead to shallower spectra and be characterized by a longer duration.

The results we find therefore strongly support the idea that the spectra of both short and long GRBs contain (at least) two separate components: a photospheric emission component that correlates directly with the inner engine activity, and a second component, possibly having a synchrotron origin, that is longer in nature and less steep.

5. Summary and Conclusion

In this work, we have selected a sample of 70 pulses from 68 short GRBs with $T_{90} < 2$ s detected by Fermi/GBM. These GRBs have at least one time bin with statistical significance $S \geqslant 15$. The time bins were selected using the Bayesian block method that ensures that the intensity does not vary strongly during an individual time bin. A total of 153 time-resolved spectra were obtained and fit with the empirical CPL spectral model, using a Bayesian statistical approach.

We investigate the distribution of the maximum (hardest) value of the spectral index α in each of the pulses, denoted α_{max}. When we assume that a single emission mechanism dominates throughout each pulse, the maximum value of the spectral index, α_{max} provides useful information on this emission mechanism. We find that 70% (within a 1σ error) of short GRBs have at least one interval in which the value of α is beyond the value allowed by the synchrotron line-of-death (see Figure 2). These values of α_{max} are typically obtained when the flux is close to its peak (see Figure 3). Therefore, the emission mechanisms in these pulses are inconsistent with being dominated by synchrotron emission.

When we consider the intervals for which $\alpha = \alpha_{max}$, we find that 36% (within a 1σ error) of the spectra are consistent with having a nondissipative photospheric origin, namely are above the NDP line (Acuner et al. 2019). This is presented in Figure 4. These numbers are slightly higher than those of long bursts. Indeed, short bursts have been found earlier to be harder than long bursts (Kouveliotou et al. 1993; Tavani 1998). These results also prove the importance of using a time-resolved spectral analysis to access the physical information of GRBs.

For the bursts compatible with a nondissipative photospheric origin, we calculate the coasting Lorentz factor, η, and find a bimodal distribution in the values of η (see Figure 5), peaking around $\sim$300 and $\sim$1000. The first peak ($\eta_{pk,1} \sim 300$) is compatible with the average Lorentz factor η found in the long GRB population (Racusin et al. 2011), while the second peak ($\eta_{pk,2} \sim 1000$) is larger by a factor of $\gtrsim$3.

A clear separation between bursts that belong to these two distinct peaks in the η distribution is further observed in their duration (T_{90}), peak energies (E_{pk}), and HR (see Figure 8). For these bursts, we further find a strong positive correlation between $\eta - E_{pk}$ and a negative correlation between $T_{90} \propto E_{pk}^{-s}$ with a power-law index $s = 0.50$ and a corresponding standard deviation 0.19 (see Figure 6).

We also find an anticorrelation between T_{90} and α_{max} when we consider a cut at high peak energy ($E_{pk} > 800$ keV), see Figure 7. This indicates that here in our sample most pulses are compatible with thermal emission at short times but with some contamination from other emission processes, such as synchrotron, at later times.

The bimodal distribution we find in the values of the Lorentz factor, together with the differences in the harness ratio, provides a strong indication that what is currently classified as short GRBs is in fact made of two separate populations. The first is an extension of the long GRB population to shorter duration, and the second is a truly separated population. A striking result is the difference in the Lorentz factors, by an average factor of $\gtrsim$3, with this separate population having a Lorentz factor of $\sim$1000 and even higher in some cases. This implies that on average, the outflows of the separate population contain much less ejected material than the outflow of long GRBs, which provides a further clue to the true nature of short GRB progenitors.

Our results provide a direct indication that the GRB duration by itself is not sufficient to classify the nature of a GRB: $T_{90} \lesssim 2$ s or $T_{90} \gtrsim 2$ s by itself is not enough to separate short and long GRBs. Rather, one needs to consider additional information, which includes spectral information, such as the hardest value of α in each pulse/burst, and the corresponding Lorentz factor, η. Indeed, the classification of GRBs has long been discussed in the literature as a way of distinguishing GRB progenitors (Kouveliotou et al. 1993; Tarnopolski 2015, and references there in). Here we show that the maximum (hardest) value of α in each pulse/burst can be used as an additional method for the classification of bursts, especially for the classification of short bursts.

These surprising results lead us to conclude the following: (1) thermal (photospheric) emission is ubiquitous among short GRBs, with $\sim$1/3 being consistent with having a pure thermal origin, and another large fraction may also have a thermal origin, which is distorted by subphotospheric energy dissipation. However, this component is often accompanied by an additional emission mechanism (likely synchrotron), which makes it hard to separate and clearly identify the dominant mechanism. (2) At early (short) times, the thermal component often dominates, but at longer times, it is accompanied by a second mechanism, which makes it subdominant. (3) Only for those bursts in which the thermal component dominates do we find a correlation between pulse (burst) duration T_{90} and the peak energy E_{pk} that corresponds to the temperature: a higher peak energy corresponds to a shorter burst duration. Because no corresponding correlation is found in the flux, this implies that a similar amount of energy is released in a short time, which leads to a higher temperature. This result may therefore provide a very strong hint toward a better understanding of the progenitor models and explosion mechanisms in short GRBs. (4) When only bursts with a high peak energy, $E_{pk} > 800$ keV, are considered, we further find a correlation between the burst duration T_{90} and the hardest spectral slope α_{max}. This further supports the idea of a dual emission mechanisms: thermal and nonthermal (synchrotron).

Facility: Fermi/GBM .

Software: 3ML (Vianello et al. 2015).

Appendix
Selection of Statistical Significance

We used the criterion that the significance S should be higher than 15 for each time bin that was analyzed and interpreted.

This criterion was found adequate to ensure that the spectral slopes and peak energies are determined with sufficient accuracy. In order to find the appropriate level of significance, we generated a large number of synthetic spectra with different peak energies. The properties of the simulated observations, such as the detector response and viewing angle, were based on the observations of GRB090820 (which had $\alpha = -0.5$), and the background spectrum was assumed to be a power law with index -1.5. The normalization of these generating models was chosen such that the significance for each spectrum attained the same value. This process was repeated for three cases $S = 10$, 15, and 20, and the distributions of the fitted spectral parameters were compared. The results showed similar parameter distributions for the two cases with $S = 15$ and 20, but the spectra became softer at lower values of S. This can be explained by the limited instrumental energy range that does not allow properly capturing the low-energy spectral slope when the value of S in the data is too low. In fact, we found that even at low values of S, a high spectral peak energy still allowed us to determine the low-energy index correctly. Because short GRBs on average have higher spectral peak energies than long GRBs (e.g., Ghirlanda et al. 2011), the criterion $S \geqslant 15$ can be used instead of the criterion $S \geqslant 20$, which was, e.g., used for long bursts in Yu et al. (2019). Therefore, the limit of $S \geqslant 15$ is necessary and enough to suppress instrumental effects and was therefore used to ensure well-constrained spectral fits in our sample of short GRBs.

ORCID iDs

Hüsne Dereli-Bégué ⓘ https://orcid.org/0000-0002-8852-7530

Asaf Pe'er ⓘ https://orcid.org/0000-0001-8667-0889

Felix Ryde ⓘ https://orcid.org/0000-0002-9769-8016

References

Abbott, B. P., Abbott, R., Abbott, T. D., et al. 2017, ApJL, 848, L13
Acuner, Z., & Ryde, F. 2018, MNRAS, 475, 1708
Acuner, Z., Ryde, F., & Yu, H.-F. 2019, MNRAS, 487, 5508
Acuner, Z., Ryde, F., Pe'er, A., et al. 2020, ApJ, 893, 128
Ahlgren, B., Larsson, J., Ahlberg, E., et al. 2019, MNRAS, 485, 474
Ahlgren, B., Larsson, J., Nymark, T., Ryde, F., & Pe'er, A. 2015, MNRAS, 454, L31
Amati, L. 2006, MNRAS, 372, 233
Axelsson, M., & Borgonovo, L. 2015, MNRAS, 447, 3150
Band, D., Matteson, J., Ford, L., et al. 1993, ApJ, 413, 281
Baring, M. G., & Braby, M. L. 2004, ApJ, 613, 460B
Bégué, D., Siutsou, I. A., & Vereshchagin, G. V. 2013, ApJ, 767, 139
Beloborodov, A. M. 2010, MNRAS, 407, 1033
Beloborodov, A. M. 2011, ApJ, 737, 68
Bissaldi, E., von Kienlin, A., Kouveliotou, C., et al. 2011, ApJ, 733, 97
Burgess, J. M., Bégué, D., Greiner, J., et al. 2019a, Natur, 4, 174
Burgess, J. M., Bégué, D., Ryde, F., et al. 2016, ApJ, 822, 63
Burgess, J. M., Greiner, J., Bégué, D., & Berlato, F. 2019b, MNRAS, 490, 927
Burgess, J. M., Preece, R. D., Baring, M. G., et al. 2011, ApJ, 741, 24
Burgess, J. M., Ryde, F., & Yu, H.-F. 2015, MNRAS, 451, 1511
Cash, W. 1979, ApJ, 228, 939
Chen, Y., Liu, R. Y., & Wang, X. Y. 2018, MNRAS, 478, 749
Eichler, D., Livio, M., Piran, T., & Schramm, D. N. 1989, Natur, 340, 126
Gelman, A., Hwang, J., & Vehtari, A 2014, Statistics and Computing, 24, 6
Ghirlanda, G., Ghisellini, G., & Nava, L. 2011, MNRAS, 418, L109
Ghirlanda, G., Nappo, F., Ghisellini, G., et al. 2018, A&A, 609, 112
Ghirlanda, G., Nava, L., Ghisellini, G., Celotti, A., & Firmani, C. 2009, A&A, 496, 585
Ghisellini, G., Ghirlanda, G., & Oganesyan, G. 2020, A&A, 636, A82
Giannios, D., & Spruit, H. C. 2005, A&A, 430, 1
Goldstein, A., Burgess, J. M., Preece, R. D., et al. 2012, ApJS, 199, 19
Goldstein, A., Veres, P., Burns, E., et al. 2017, ApJL, 848, L14
Goodman, J. 1986, ApJL, 308, L47
Gruber, D., Goldstein, A., Weller von Ahlefeld, V., et al. 2014, ApJS, 211, 12
Hakkila, J., & Preece, R. D. 2011, ApJ, 740, 104
Hartigan, J. A., & Hartigan, P. M. 1985, AnSta, 13, 70
Howell, E. J., & Coward, D. M. 2013, MNRAS, 428, 167
Ito, H., Nagataki, S., Ono, M., et al. 2013, ApJ, 777, 62
Kaneko, Y., Preece, R. D., Briggs, M. S., et al. 2006, ApJS, 166, 298
Kelly, B. C. 2007, ApJ, 665, 1489
Kouveliotou, C., Meegan, C. A., Fishman, G. J., et al. 1993, ApJL, 413, L101
Lloyd, N. M., & Petrosian, V. 2000, ApJ, 543, 722
Lundman, C., Pe'er, A., & Ryde, F. 2013, MNRAS, 428, 2430
Mészáros, P. 2006, RPPh, 69, 2259
Norris, J. P., Gehrels, N., & Scargle, J. D. 2011, ApJ, 735, 23
Oganesyan, G., Nava, L., Ghirlanda, G., et al. 2019, A&A, 628, A59
Paczynski, B. 1986, ApJL, 308, L43
Pe'er, A., Mészáros, P., & Rees, M. J. 2006, ApJ, 652, 482
Pe'er, A., Ryde, F., Wijers, R. A. M. J., et al. 2007, ApJL, 664, L1
Preece, R. D., Briggs, M. S., Mallozzi, R. S., et al. 1998, ApJL, 506, L23
Qin, Y., Liang, E. W., Liang, Y. F., et al. 2013, ApJ, 763, 15
Racusin, J. L., Oates, S. R., Schady, R., et al. 2011, ApJ, 738, 138
Richardson, G., Koshut, T., Paciesas, W., & Kouveliotou, C. 1996, in AIP Conf. Ser. 384, Gamma-ray bursts, ed. C. Kouveliotou, M. F. Briggs, & J. G. Fishman (Melville, NY: AIP), 87
Ryde, F. 1999, ApL&C, 39, 281
Ryde, F. 2004, ApJ, 614, 827
Ryde, F., Lundman, C., & Acuner, Z. 2017, MNRAS, 472, 1897
Ryde, F., Yu, H.-F., Dereli-Bégué, H., et al. 2019, MNRAS, 484, 1912
Scargle, J. D., Norris, J. P., Jackson, B., & Chiang, J. 2013, arXiv:1304.2818
Silverman, B. W. 1986, Monographs on Statistics and Applied Probability (London: Chapman and Hall)
Spiegelhalter, D. J., Best, N. G., Carlin, B. P., & van der Linde, A. 2002, J.R. Statist. Soc. B, 64, 583
Tarnopolski, M. 2015, A&A, 581, A29
Tavani, M. 1998, ApJL, 497, L21
Vianello, G. 2018, ApJS, 236, 17
Vianello, G., Gill, R., Granot, J., et al. 2018, ApJ, 864, 163
Vianello, G., Lauer, R. J., Younk, P., et al. 2015, arXiv:1507.08343
von Kienlin, A., Meegan, C. A., Paciesas, W. S., et al. 2014, ApJS, 211, 13
Woosley, S. E. 1993, ApJ, 405, 273
Yonetoku, D., Murakami, T., Nakamura, T., et al. 2004, ApJ, 609, 935
Yu, H.-F., Dereli-Bégué, H., & Ryde, F. 2019, ApJ, 886, 20
Yu, H.-F., Preece, R. D., Greiner, J., et al. 2016, A&A, 588, A135
Yu, H.-F., van Eerten, H. J., Greiner, J., et al. 2015, A&A, 583, A129
Zhang, B.-B., Zhang, B., Castro-Tirado, A. J., et al. 2018, NatAs, 2, 69